Investigating the Multicentennial Oscillation of the AMOC Using a Simplified Two-Dimensional Ocean Model

Shuxiang Wang, Haijun Yang*, and Xiangying Zhou

Department of Atmospheric and Oceanic Sciences and Institute of Atmospheric Science, Fudan University, Shanghai 200438, China

Key Laboratory of Polar Atmosphere-ocean-ice System for Weather and Climate of Ministry of Education, Fudan University, Shanghai 200438, China

Climate Dynamics

1st submission, March 25, 2025

Corresponding author: Haijun Yang, yanghj@fudan.edu.cn

ABSTRACT

The Atlantic Meridional Overturning Circulation (AMOC) exhibits significant multicentennial oscillations (MCO), playing a crucial role in long-term climate variability. In this study, we use a simplified two-dimensional ocean model to extend previous theoretical and coupled model studies on AMOC MCO, providing clearer physical insights and bridging the gap between idealized and high-complexity numerical models. Our results demonstrate that stochastic salinity forcing effectively excites AMOC MCO, with the oscillation primarily driven by the tropical-subpolar advection feedback. Through sensitivity experiments, we find that the period of the AMOC MCO is largely controlled by the strength and vertical structure of the climatological AMOC: a stronger AMOC shortens the oscillation period, whereas a deeper AMOC maximum extends it. Under weak AMOC conditions, the oscillation timescale can extend to millennial scales. Additionally, we explore the influence of wind-driven circulation and find that while it has little effect on the MCO period, it slightly modifies the amplitude of variability by suppressing low-frequency components and enhancing high-frequency fluctuations. The use of a simplified model enables a systematic exploration of key physical mechanisms governing AMOC MCO, offering valuable insights into long-term climate variability.

KEYWORDS: Atlantic Meridional Overturning Circulation, Multicentennial Oscillation, Two-Dimensional Ocean Model, Stochastic Forcing, Wind-driven Circulation

1. Introduction

The Earth's climate system exhibits variability across a wide range of timescales. Extensive proxy records from tree rings, ice cores, and lakebed or seabed sediments indicate the presence of centennial-to-millennial-scale climate variabilities in the climate system (Chapman and Shackleton 2000; McDermott et al. 2001; Proctor et al. 2002; Newby et al. 2014; Askjær et al. 2022). The multicentennial oscillation (MCO) may have influenced the evolution of historical human civilizations and the rise and fall of dynasties (Hodell et al. 1995; Binford et al. 1997). In-depth studies on the MCO not only has profound implications for the understanding of ancient civilizations, but also enhances our capability of the long-term future climate projection (Collins and Sinha 2003).

Since external forcings are relatively stable during the Holocene period, internal variability may be the dominant component of the multicentennial variability. Studies also suggested that during the past two millennia the forced signal accounts for only 10–35% of the total variance of signals lasting over 10 years (Moffa-Sánchez et al. 2019). Among the components of the Earth system, the ocean, due to its immense thermal inertia, is capable of sustaining long time-scale internal variabilities. As a crucial part of ocean circulation, the Atlantic Meridional Overturning Circulation (AMOC) has a timescale that can extend to thousands of years, making it a potential driver of the MCO. Consequently, understanding the multicentennial variability of AMOC has become a significant research focus in the field of long-term climate variability (Stocker and Mysak 1992; Rahmstorf 2002; Oppo et al. 2003; Rahmstorf 2006; Msadek and Frankignoul 2009; Srokosz et al. 2012; Kissel et al. 2013; Thornalley et al. 2013; Chabaud et al. 2014).

In the absence of long-term direct observations of AMOC at this timescale, studies on the AMOC have predominantly relied on models of varying complexity (Stommel 1961; Welander 1982; Mikolajewicz and Maier-Reimer 1990; Stocker et al. 1992; Mysak et al. 1993; Roebber 1995; Walland et al. 2000; Askjær et al. 2022; Cao et al. 2023). Recent studies have demonstrated that the generation and maintenance of AMOC MCO can be investigated more clearly using simple theoretical models. For instance, a four-box ocean model considering only salinity has been employed to identify and explain the oscillation mechanism of AMOC MCO from a linear perspective (Li and Yang 2022). This study revealed that the oscillation period is associated with the turnover time of the ocean, which is in turn determined by the AMOC strength and the volume of upper ocean. Stochastic freshwater forcing can trigger this oscillation. Subsequent research expands on this by examining the stabilizing role of temperature in AMOC MCO, and refining the advection feedback mechanism by incorporating both the salinity and temperature. Specifically, to fulfill the AMOC MCO, both positive feedbacks from perturbation advection of mean salinity and mean advection of temperature anomaly and negative feedbacks from mean advection of salinity anomaly and perturbation advection of mean temperature are needed, and they have to work together organically.

Early studies using both two-dimensional and three-dimensional ocean models have produced the AMOC MCO (Mikolajewicz and Maier-Reimer 1990; Mysak et al. 1993). However, these studies primarily focused on the effect of mean advection mechanism of salinity anomaly, neglecting the perturbation advection mechanism of mean salinity. Some two-dimensional models explored variations in oscillation periods related to diffusive thermal and saline processes, but did not deliberate how changes in diffusion coefficients affect the AMOC structure (Mysak et al. 1993; Schmidt and Mysak 1996). Later, complex coupled models are used to investigate the AMOC MCO, with its origin emerging as a key topic. Different models give the varying explanations regarding the origin of the AMOC MCO. The AMOC MCO could be originated in the North Atlantic (Yang et al. 2024b), the Arctic Ocean (Jiang et al. 2021; Meccia et al. 2022; Mehling et al. 2022), or the Southern Ocean (Park and Latif 2008; Delworth and Zeng 2012). More recently, coupled model studies argue that the North Atlantic related processes dominate the origin of AMOC MCO and highlight the role of positive feedback of perturbation advection of mean salinity, which was overlooked in earlier modeling efforts (Yang et al. 2024b).

This work is part of our serial studies on the AMOC MCO. We use the two-dimensional ocean model, trying the fill the gap between theoretical models and the coupled models and providing clearer physical explanations with more sensitivity experiments. Our previous theoretical studies on the AMOC MCO using box models (Li and Yang 2022; Yang et al. 2024a) have pinpointed the main positive and negative feedback processes leading to the AMOC MCO. Building on this foundation, the two-dimensional ocean model can capture more detailed features, providing a more comprehensive depiction of AMOC variability. Compared to coupled climate models, the two-dimensional model significantly reduces computational costs and a large amount of sensitivity experiments can be easily conducted, which facilitate an in-depth exploration of the effects of various parameters and forcing conditions on the AMOC MCO.

The paper is organized as follows. Section 2 introduces the two-dimensional ocean model, and how to obtain a reasonable AMOC. Section 3 examines the role of stochastic freshwater forcing in triggering the AMOC MCO and analyzes the advection feedback mechanism. Section 4 investigates the factors influencing the period of AMOC MCO, including the strength and structure of AMOC. Furthermore, the study explores the impact of wind-driven circulation on the MCO in Section 5. Section 6 is summary and discussion. By employing the simplified ocean model, this study seeks to provide novel insights into the multicentennial variability of the climate system and highlight the critical role of AMOC in shaping historical climate patterns.

2. Two-dimensional ocean model

A simple two-dimensional ocean model is used to study the AMOC MCO in this work. This zonal-averaged two-dimensional model is based on that used by Marotzke et al. (1988), but is supplemented by horizontal mixing and diffusion terms in this work. The model equations are written as follows:

$$A_V \frac{\partial^4 \psi}{\partial z^4} + A_H \frac{\partial^4 \psi}{\partial y^2 \partial z^2} = g\left(-\alpha \frac{\partial T}{\partial y} + \beta \frac{\partial S}{\partial y}\right) \tag{1}$$

$$\frac{\partial T}{\partial t} + v\frac{\partial T}{\partial y} + w\frac{\partial T}{\partial z} = K_H \frac{\partial^2 T}{\partial y^2} + K_V \frac{\partial^2 T}{\partial z^2} \tag{2}$$

$$\frac{\partial S}{\partial t} + v\frac{\partial S}{\partial y} + w\frac{\partial S}{\partial z} = K_H \frac{\partial^2 S}{\partial y^2} + K_V \frac{\partial^2 S}{\partial z^2} \tag{3}$$

Here, A_V and A_H are vertical and horizonal eddy viscosity coefficients, respectively. K_V and K_H are vertical and horizonal diffusion coefficients, respectively. α and β are thermal contraction and saline expansion coefficients, respectively. ψ is the mass streamfunction representing the AMOC in this model, which is diagnosed from temperature (T) and salinity (S) distributions. $v = -\frac{\partial \psi}{\partial z}$ and $w = \frac{\partial \psi}{\partial y}$, which are meridional and vertical velocity, respectively. T and S are calculated through time-forward integration, forced by the surface buoyance boundary condition. The lateral boundary conditions are assumed be of no normal flow for ψ and no heat (salt) flux for $T(S)$. The bottom boundary conditions are of non-slip for ψ and also no flux for T and S.

For the spin-up experiment, the restored surface boundary conditions are used for both T and S:

$$Q_H = \frac{\Delta Z}{\tau}(T_0 - T), \quad \mathrm{Q_S} = \frac{\Delta Z}{\tau}(S_0 - S) \tag{4a}$$

$$T_0 = T_L + T_*\left(1 + \cos\frac{\pi y}{L}\right), \quad S_0 = S_L + S_*\left(1 + \cos\frac{\pi y}{L}\right) \tag{4b}$$

For the all-subsequent experiments after the spin-up, the mixed boundary conditions, i.e., restored surface condition for T and flux condition for S are used:

$$Q_H = \frac{\Delta Z}{\tau}(T_0 - T), \quad Q_S = Q_S(y) \tag{4c}$$

where ΔZ is the depth of the top layer of the ocean, T_0 and S_0 are prescribed sea surface temperature (SST) and salinity (SSS), $T_L = 0$℃ and $S_L = 35\ psu$ are the reference temperature and salinity of the polar regions, respectively, $S_* = 1\ psu$, $T_* = 12.5$℃. τ is relaxation timescale for heat and salinity, which is given as 1 year in this work. L is the meridional length of the hemispheric basin. Once the equilibrium S is obtained through the spin-up experiment, the virtual surface salinity flux $Q_S(y)$ in (4c), which maintains this equilibrium, can be diagnosed from the surface salinity distribution. The meridional integration of $Q_S(y)$ is zero, ensuring the salinity conservation.

In this study, the model domain extends from 70°S to 70°N, with a depth of 5000 m and a width of 6000 km. This configuration is used to simulate the thermohaline circulation in the Atlantic Ocean. The spin-up experiment is integrated for 5000 years with a time step of 30 days. The parameter settings of the model are shown in Table 1. In this study, the AMOC index is defined as the maximum streamfunction in the North Atlantic spanning 20°–70°N and 200–3000 m.

TABLE. 1. Simple model parameters in this study

Symbol	Physical meaning	Value
L, W, D	Hemispheric basin length, width and depth	7770 km, 6000 km, 5000 m
α, β	Thermal expansion and haline contraction coefficient	1.468×10^{-4}/°C, 7.61×10^{-4}/psu
$M \times N$	Horizontal and vertical grid points	32×17
A_V, A_H	Vertical and horizontal eddy viscosity coefficient	15 $m^2\ s^{-1}$, $2.0\times10^9\ m^2\ s^{-1}$
K_V, K_H	Vertical and horizontal diffusion coefficient	$2.1\times10^{-4}\ m^2\ s^{-1}$, $3\times10^3\ m^2\ s^{-1}$

After the 5000-year spin-up integration under the restored surface boundary condition (Eqs. (4a-b)), a 5000-year control experiment is then conducted under the mixed boundary condition (Eq. (4c)), with the parameters listed in Table 1. The 5000 years integration ensures the model reaching its equilibrium state. The equilibrium temperature, salinity and streamfunction are shown in Figure 1. The equilibrium gradients of temperature and salinity are greater in the upper layers and smaller in the deeper layers. Under symmetric boundary conditions, the maximum temperature is in the equatorial region, while the maximum salinity is between the equator and 30°N, extending downward to about 1500 m (Figs. 1a-b). The AMOC exhibits a single-cell structure spanning from pole to pole (Fig. 1c), consistent with previous studies (Marotzke et al. 1988; Stocker et al. 1992; Yang and Neelin 1993), and closely resembling the climatological AMOC in coupled models (Hirschi et al. 2020; Yang et al. 2024b). The AMOC has the maximum value of about 20 Sv at 40°N that locates at the depth of 1500 m. Note that a non-uniform vertical axis is used in Figs. 1a-c, to exhibit more clearly the upper structure of temperature, salinity and AMOC, in which the upper ocean is exaggerated. For reference, the AMOC on regular vertical axis is plotted in Fig. 1d.

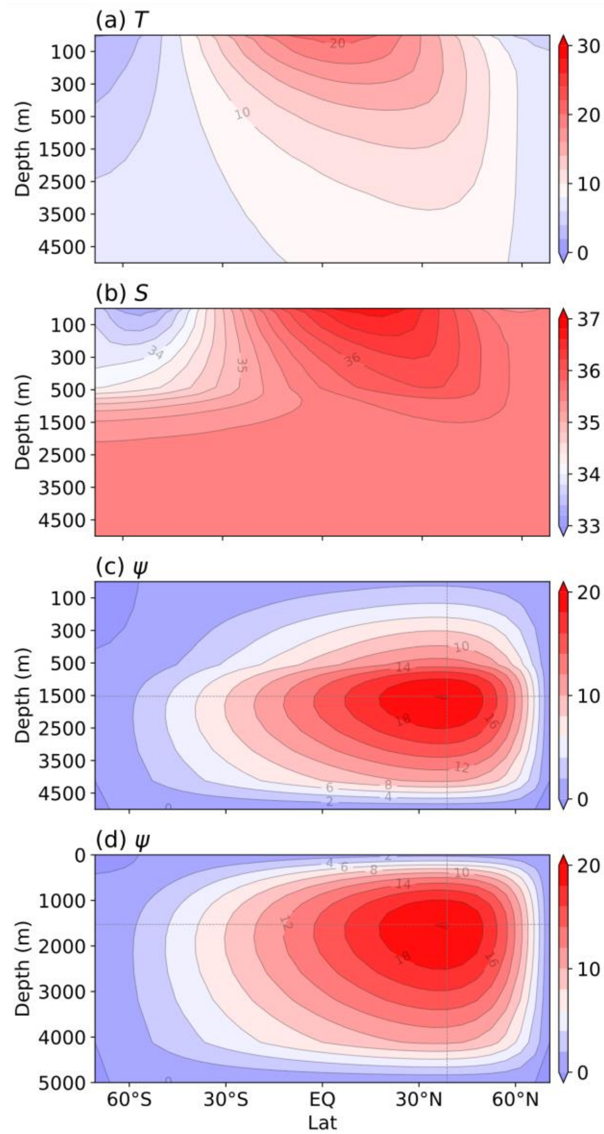

FIG. 1. Equilibrium (a) Temperature (units: °C), (b) Salinity (units: psu) and (c)-(d) Streamfunction (units: Sv; 1 Sv = 10^6 m^3 s^{-1}) in the control run. Note that (c) and (d) are the same, except using different vertical axis. Gray dotted lines in (c)-(d) cross the point of the maximum value of the streamfunction, which divide the ocean basin into 4 sub-basins: the upper and lower subpolar ocean in the Northern Hemisphere, the upper and lower ocean in the tropics and Southern Hemisphere, representing the deep-water formation region of the AMOC and the regions for the upper northward (lower southward) branch of the AMOC, respectively.

3. MCO in the two-dimensional model

a. Stochastic experiment

The AMOC can exhibit multicentennial oscillation when the model is forced by stochastic freshwater flux. With the inclusion of stochastic freshwater, Eq. (3) is rewritten as follows:

$$\frac{\partial S}{\partial t} + v\frac{\partial S}{\partial y} + w\frac{\partial S}{\partial z} = K_H\frac{\partial^2 S}{\partial y^2} + K_V\frac{\partial^2 S}{\partial z^2} + N \quad (5)$$

where N represents the external stochastic forcing, which is generated by a first-order autoregressive model:

$$N_{k+1} = aN_k + bG_k \quad (6)$$

The perturbation N in the k+1 year is generated from the k year and a standard Gaussian random variable G_k. Here, a is set to 0, 0.368 and 0.905 respectively, corresponding to e-folding times of the autocovariance function of 0 (white noise), 1 year and 10 years (red noise), respectively. Meanwhile, b is set to 0.28, 0.35 and 0.084 psu yr^{-1}, which are chosen to constrain the magnitude of AMOC variability within 5 Sv.

For the experiments with stochastic forcing, the stochastic freshwater flux is added only in the subpolar region of the Northern Hemisphere (around 40°N ~ 50°N). The climatological state of the control run is used as the initial condition. The stochastic experiments are integrated for 5000 years. For each form of noise pattern (white and red noises), 50 ensemble experiments are conducted with 50 different noises that are generated in advance. The last 4500 years annual mean data are used for analyses.

Multicentennial oscillation can be successfully excited by the stochastic freshwater forcing. Figure 2 shows the timeseries of AMOC index, which exhibits sustained MCO under stochastic forcing. Regardless of the forms of noise pattern, the MCO is always remarkable, except that the AMOC under white noise forcing (Fig. 2a) exhibits slightly more high-frequency component than the AMOC under red noise forcing (Fig. 2c). Here, we would like to emphasize that no temporal filter has been applied to the AMOC timeseries in Fig.2. The SSS and SST in the subpolar North Atlantic vary almost synchronously with the AMOC index (Fig. 3a), also exhibiting a remarkable MCO. The SSS changes lead the AMOC by approximately 5–10 years (Fig. 3b), suggesting the driving effect of SSS on the AMOC. The MCO is the first principal mode, because in the two-dimensional ocean model there is no wave dynamics, and thus variabilities from interannual to multi-decadal timescale are automatically filtered.

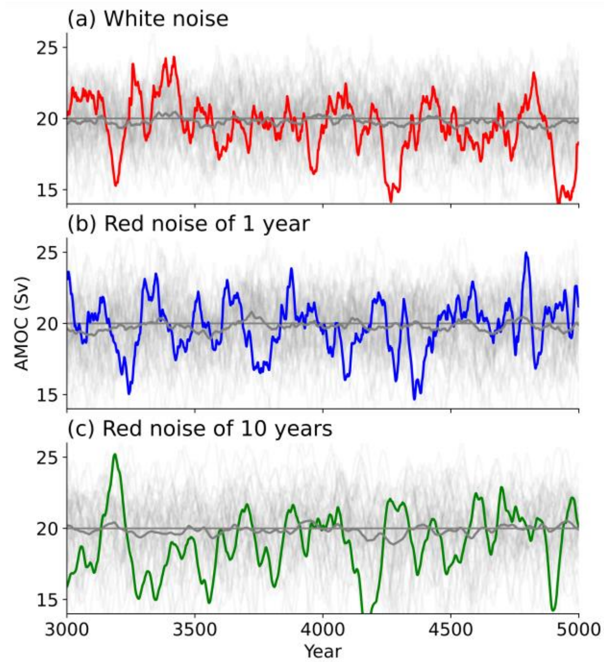

FIG. 2. (a) Time series of AMOC index (units: Sv) in the two-dimensional ocean model, under white-noise forcing. The AMOC index is defined by the maximum streamfunction in the North Atlantic. (b)-(c) are the same as (a), but forced by red noises with 1-year and 10-year e-folding time, respectively. In (a)-(c), thin gray curves represent 50 individual experiments, while ensemble means are represented by thick gray curves. Thick red, blue and green curves represent one realization of 50 ensemble experiments. For clearness, only 2000 years data are used to plot the timeseries. No temporal filter is applied to these curves.

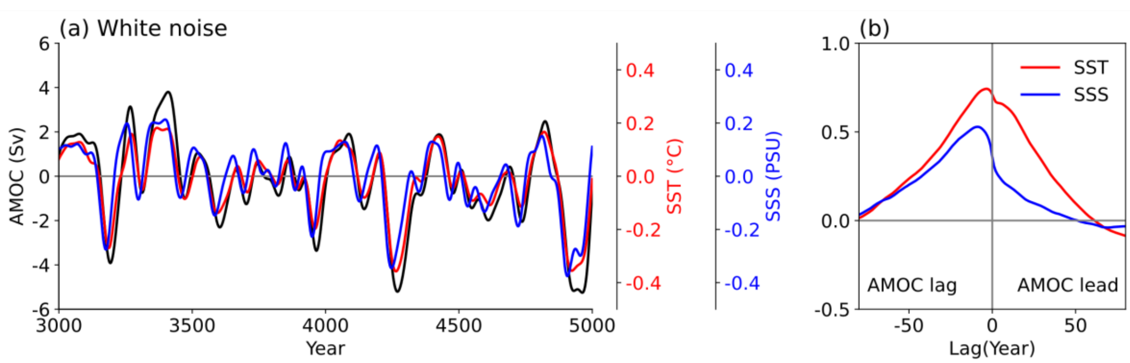

FIG. 3. (a) Time series of anomalous AMOC index (black, units: Sv), anomalous sea surface salinity (SSS) (blue, units: psu) and sea surface temperature (SST) (red, units: °C) in the two-dimensional ocean model, under white-noise forcing. The SSS and SST are averaged over 40°-50°N. A temporal filter with 60-year running mean is applied to these curves. (b) Lead and lag correlation coefficients of SSS (blue) and SST (red) anomalies on the AMOC index. Negative lag means the AMOC lags SSS/SST anomalies (units: years). Data used here are the same experiment as in Fig. 2a.

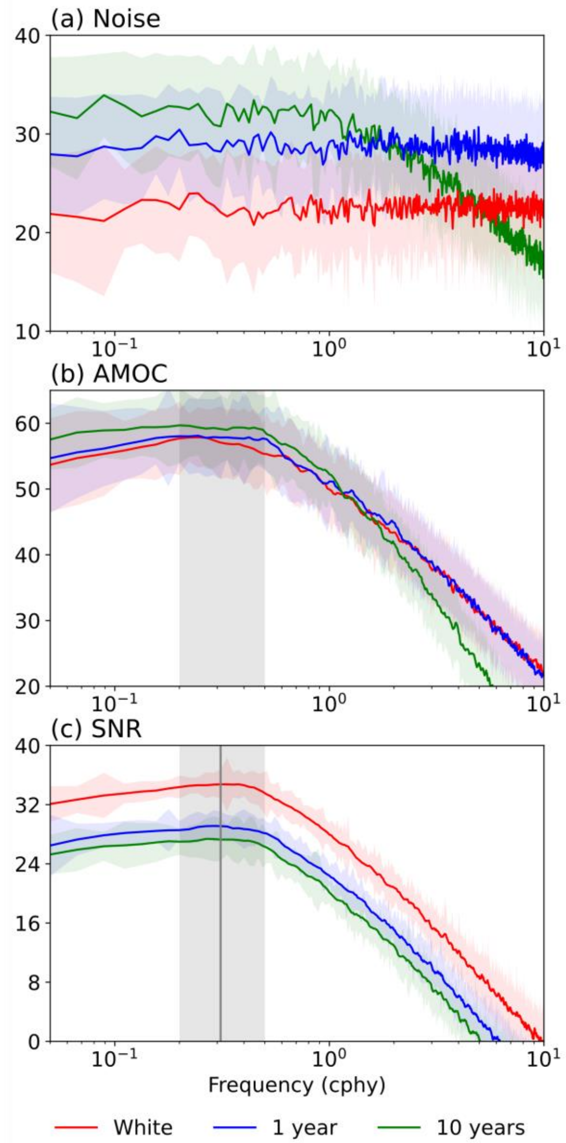

FIG. 4. Power spectra (units: dB) of (a) the noise and (b) the AMOC index. (c) The ratios of the AMOC spectrum to the noise spectrum (units: dB), i.e., signal-noise ratio (SNR), with peaks around 0.2-0.5 cphy (200-500 years) that are specified by pale-gray shadow. Thick red, blue and green curves represent the ensemble mean of 50 realizations that forced by white noise, red noises with 1-year and 10-year e-folding time, respectively, and pale shadows of red, blue and green demonstrate the spread of the 50 realizations. The x-coordinate represents frequency with unit of cycles per hundred year (cphy).

The MCO is further examined by power spectrum of the forced AMOC index (Fig. 4). The ratio of the AMOC spectrum (Fig. 4b) to the spectrum of stochastic freshwater flux (Fig. 4a) is shown in

Fig. 4c, which illustrates that the AMOC responds most efficiently to the noise with a period between 250-500 years. The forms of noise (white noise or red noise) do not affect the MCO period, but do affect the MCO amplitude marginally (Fig. 4c), with that under white noise forcing stronger than that under red noise forcing. Note that the power spectrum analyses in Fig. 4 are for 50 ensemble experiments, not just for one realization shown in Fig. 2. In general, Fig. 4 suggests that the MCO in the two-dimensional ocean model may be an intrinsic feature of the Atlantic Ocean, independent of external forcing. This finding aligns closely with conclusions from previous theoretical research using 4-box ocean model (Li and Yang 2022).

b. Evolution of MCO in the simple model

In this section, evolutions of salinity and temperature anomalies with the AMOC over multicentennial cycle are analyzed. Figure 5 illustrates the lead/lag regression coefficients of salinity anomalies on the AMOC index, overlaid with climatological potential density calculated from temperature and salinity. Positive and negative regression coefficients at a lag of n years indicate the presence of positive and negative salinity anomalies, respectively, in the corresponding regions when salinity anomalies lag the AMOC by n years. For the convenience next, we state positive/negative regression coefficient as positive/negative salinity anomaly. Lag -150 and 0 years can be roughly regarded as the peak years of the negative and positive AMOC anomalies, given the MCO period of about 300 years. Data used in Fig. 5 are from the same one realization of 50 ensemble experiments under white noise forcing (Fig. 2a).

When the AMOC is at the positive peak (Fig. 5f), there is a clear maximum positive salinity anomaly in the upper ocean near 50°N, corresponding to the strongest North Atlantic Deep Water (NADW) formation and AMOC. The positive anomaly extends downward from the surface ocean north of 30°N to the deep ocean, and is then advected southward by the lower branch of the AMOC (Figs. 5g-i). To the south of the subpolar region, there is generally negative anomaly above 1500 m in the tropical ocean, which is advected northward by the upper branch of the AMOC, and can ultimately result in the phase change in the subpolar ocean (Figs. 5g-l). Similarly, during the 200-0 years when salinity anomalies lead the AMOC (Figs. 5a-f), negative salinity anomalies appear north of 50°N, with the AMOC in its weak phase. Concurrently, positive salinity anomalies in the tropical upper ocean propagate northward, increasing the density in the NADW formation region and resulting in phase change in the AMOC. The upper-ocean dipole structure of salinity anomalies persists throughout its evolution, exhibiting a periodicity of phase transitions spanning multiple centuries. This structure circulates in the tropical-subpolar North Atlantic, while in the South Atlantic, salinity anomalies do not reflect evolution synchronously with the AMOC.

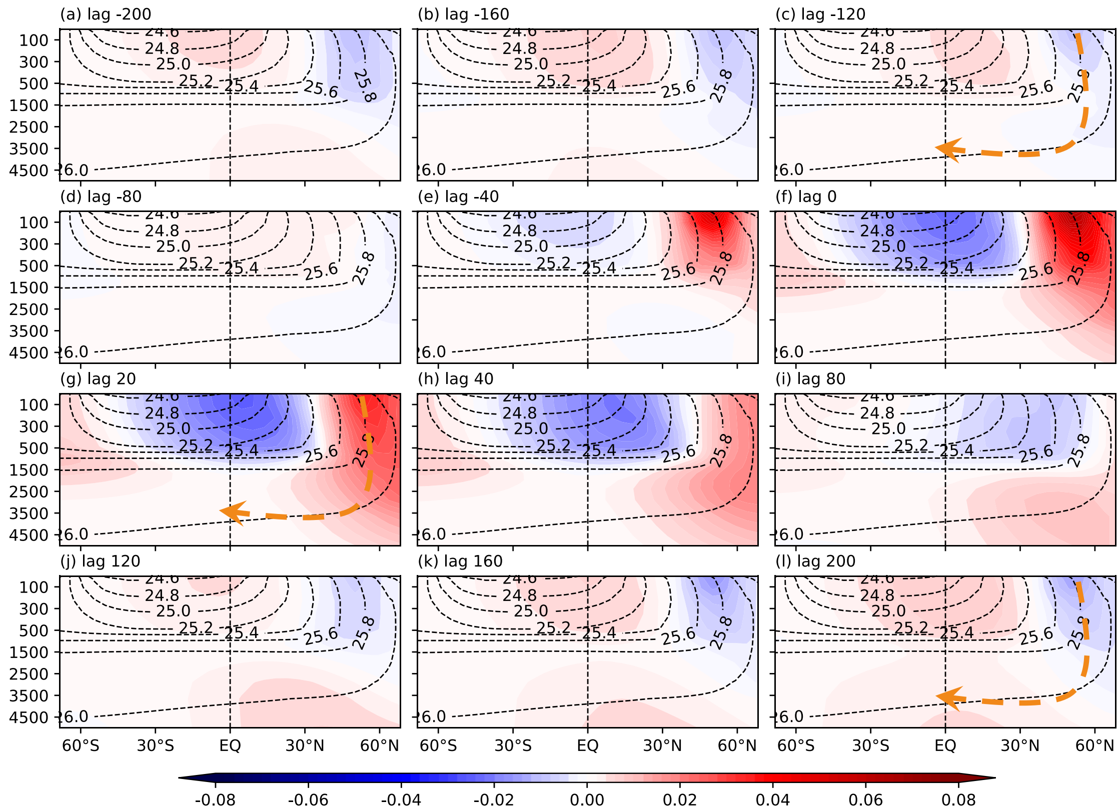

FIG. 5. Lead and lag regression coefficients of salinity anomalies on the anomalous AMOC index (shading; units: psu per Sv). Negative lag means the AMOC lags the salinity anomalies (units: years). Contours show the climatological potential density (units: kg m^{-3}). The regression coefficients were tested and found to be statistically significant at the 95% confidence level. Orange dashed arrows in (c), (g), and (l) show schematically the downward and southward movements of salinity anomalies. Data used in here are from one realization of 50 ensemble experiments under white noise forcing.

The temperature anomalies exhibit similar evolution to that of salinity anomalies (Fig. 6). The upper-ocean dipole structure of temperature anomalies is also obvious in the tropical-subpolar North Atlantic throughout its evolution. When the AMOC is in its negative phase (Figs. 6a-d), positive temperature anomaly is transported to the subpolar ocean, which tends to reduce the NADW formation and thus the AMOC. At lag 0 year, the positive temperature anomaly in the subpolar ocean reaches the maximum, concurrent with the strongest AMOC (Fig. 6f). Combined with Fig. 5f, we can conclude that it is the salinity anomalies that dominate the evolution of the AMOC, while the temperature anomalies tend to compensate the effect of the salinity anomalies on the AMOC. Comparing Fig. 6 with Fig. 5, it is noted that the most pronounced temperature anomaly in the tropics occurs at intermediate depths (Figs. 6f–i), whereas the most significant salinity anomaly is found in the upper ocean (Figs. 5f–i). This reflects constraining effect of the surface restoring boundary condition on the surface SST variability.

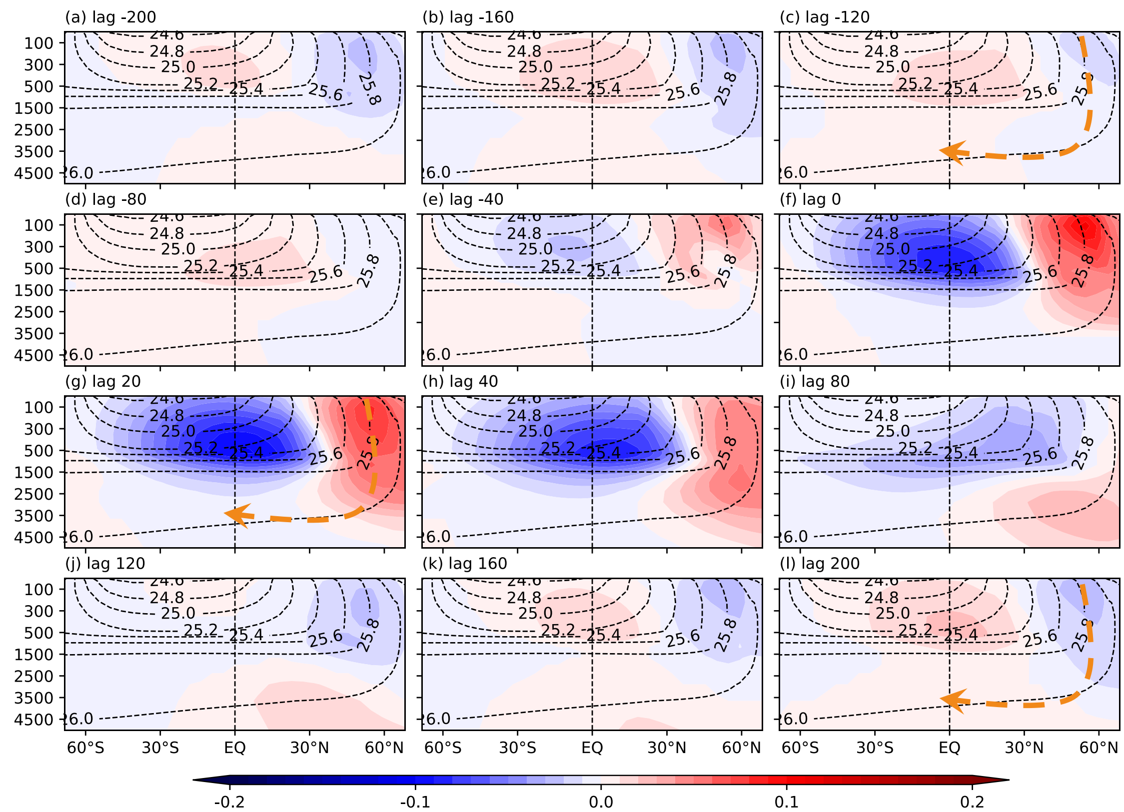

FIG. 6. Same as Fig. 5, but for temperature anomalies on the AMOC index (shading; units: °C per Sv).

To see more clearly the propagation of salinity and temperature anomalies, we average the anomalies vertically over three different depths and then calculate their lead/lag regression coefficients on the AMOC index anomaly. Figure 7 illustrates the local development of anomalies in the upper ocean of subpolar North Atlantic (Fig. 7a), the northward propagation of anomalies in the intermediate tropical ocean (Fig. 7b), as well as the southward propagation of anomalies in the deep ocean (Fig. 7c). In the upper and intermediate ocean (Figs. 7a-b), the most remarkable signal is between 35°-65°N, showing a local periodic evolution without a robust connection with signals in the lower latitudes. The maximum positive regression coefficient in the subpolar region occurs when the salinity anomalies lead the AMOC by a couple of years (denoted by orange dot in Figs. 7a-b).

Meanwhile, the maximum negative signals in the tropical ocean show a systemically northward propagation (denoted by white dashed arrows in Figs. 7a-b), with the signals lagging the AMOC sequentially by about 15-20 years from surface ocean to intermediate ocean. In the deep ocean, anomalies propagate southward from subpolar to the South Atlantic, which occurs when the AMOC leads by about 20 years (white dashed arrow in Fig. 7c).

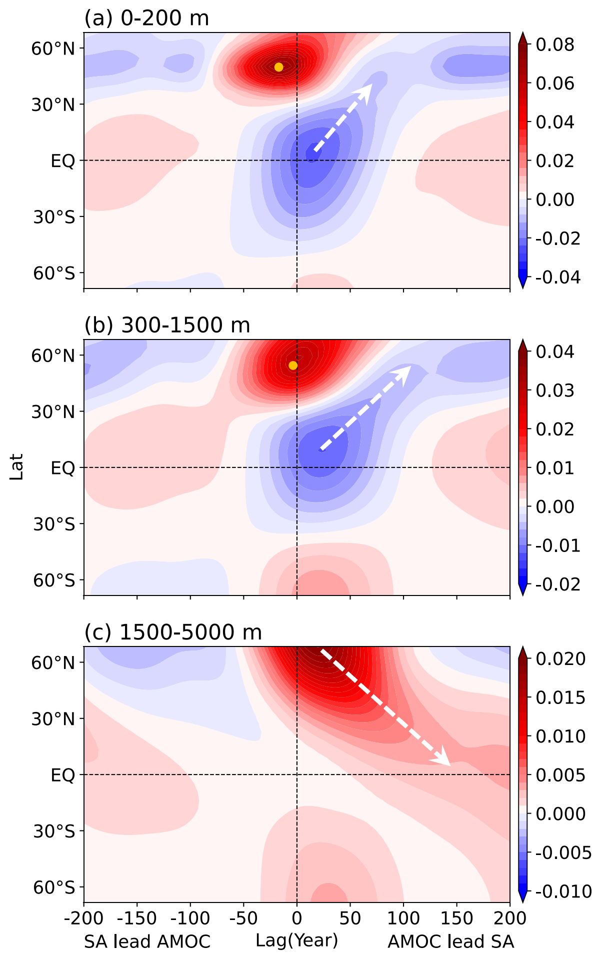

FIG. 7. Lead and lag regression coefficients of vertically averaged salinity anomalies on the low-pass filtered AMOC anomaly (shading; units: psu per Sv). (a) Averaged over 0-300 m, (b) averaged over 300-1500 m and (c) averaged over 1500-4500 m. The orange dot in (a)-(b) denotes the position of the maximum regression coefficient. The dashed white arrows in (a)-(c) show schematically the meridional propagations of salinity anomalies. Negative lag means the AMOC lags the salinity anomalies (units: year). The regression coefficients were tested and found to be statistically significant at the 95% confidence level.

Here we would like to emphasize that both the downward and southward propagation of the anomalous signal in the subpolar ocean (e.g., Figs. 5c, 5g, 7c), and the northward propagation of the anomalous signal in the tropical ocean (Figs. 7a, b) play as negative feedback in the AMOC MCO. These anomalous signals are fulfilled by the mean circulation. The local development of signals in the subpolar ocean (Fig. 7a) needs process having positive feedback, which can be provided by the perturbation advection of mean salinity gradient (Mikolajewicz and Maier-Reimer 1990; Mysak et al. 1993).

Figure 8 shows the mean salinity pattern as well the lead/lag regression of the anomalous circulation on the AMOC index. It is noticed that during the weak phase of the AMOC (Figs. 8a-d), the southward velocity anomalies hinder the northward transport of saline water from the tropics to the subpolar ocean, amplifying the negative salinity anomalies in the subpolar ocean, and leading to the further weakening of the AMOC. Similarly, during the strong phase of the AMOC (Figs. 8e-h), the northward velocity anomalies enhance the northward transport of saline water, contributing to the local development of the salinity anomalies in the subpolar ocean and the further strengthening of the AMOC. This perturbation advection of mean salinity provides a positive feedback mechanism in the AMOC MCO. A similar process applies to the mean temperature (figure not shown) simultaneously, but acts as a negative feedback mechanism. The positive and negative feedbacks identified here are consistent with recent theoretical studies using box models (Li and Yang. 2022; Yang et al. 2024a), as well as the studies using coupled models (Yang et al. 2024b).

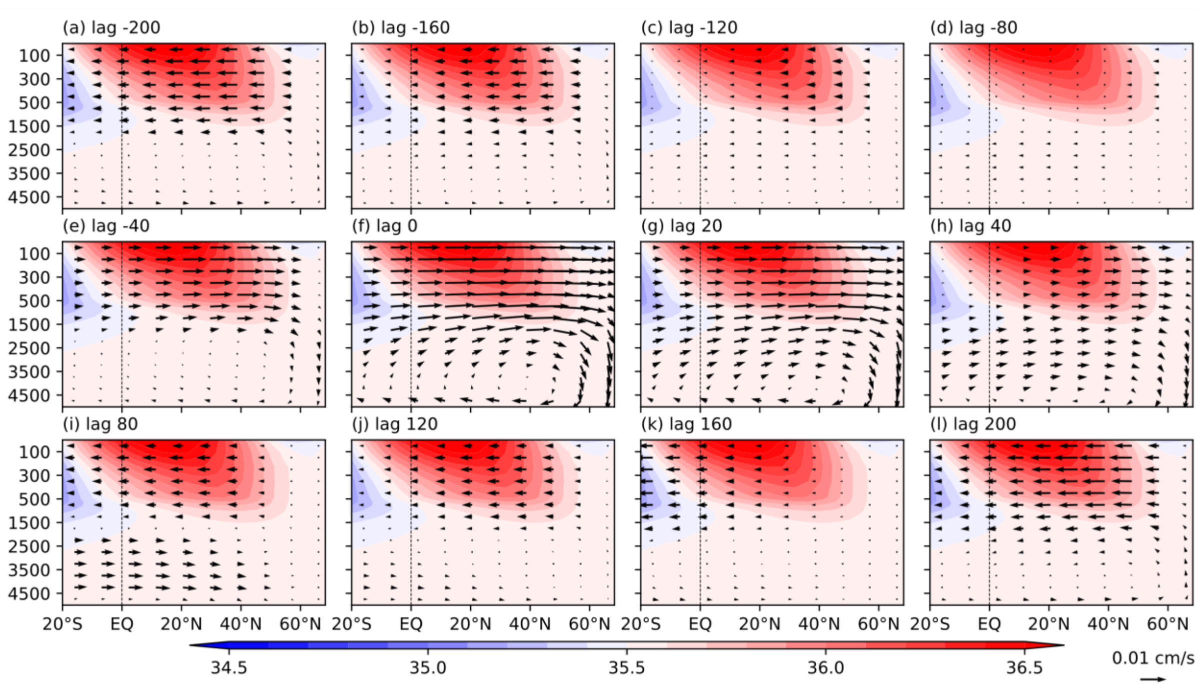

FIG. 8. Lead and lag regression coefficients of circulation on the AMOC index anomaly (vectors; units: cm/s per Sv). Negative lag means the AMOC lags the anomalous circulation (units: years). The vertical component *w* of

vectors is amplified by 10 times, in order to see the overturning circulation more clearly. Shading shows the climatological salinity. The regression coefficients were tested and found to be statistically significant at the 95% confidence level.

4. Determinant factors of the AMOC MCO

In this section we investigate how the strength and structure of climatological AMOC affect the period of the MCO. The AMOC strength and structure are defined by the value and position of the streamfunction maximum in the North Atlantic, respectively. The climatological AMOC in the control run (Fig. 1c) has the strength of about 20 Sv and the structure that the maximum is located at depth of about 1500 m (denoted by the horizontal gray dotted line in Fig. 1c). This 1500-m isobath roughly divides the ocean into the upper ocean and the lower ocean. Previous theoretical studies suggested that the MCO period can be roughly considered as the water's turnover time of the ocean basin (Li and Yang 2022), which is proportional to the total volume of upper ocean and inversely proportional to the mean strength of AMOC. This recognition from theoretical studies is hardly verified in coupled climate models because it would be too resource-consumed to conduct sensitivity experiments, however, it will be easily examined using two-dimensional model in this work.

The strength and structure of climatological AMOC can be readily regulated by eddy viscosity coefficients (A_V, A_H) and diffusion coefficients (K_V, K_H) in the two-dimensional ocean model. The climatolgical AMOC in the control run (Fig. 1c) is obtained under values in Table 1. By deliberately chosing the values of A_V, A_H, K_V and K_H (Table 2), we can have four different equilibriums (Fig. 9): (1) the strong and shallow AMOC, with the strength of about 30 Sv and the location of the maximum at about 1000 m depth (Fig. 9a3); (2) the weak and shallow one, with the strength of about 10 Sv and the location of the maximum at about 1000 m (Fig. 9b3); (3) the strong and deep one, with the strength of about 30 Sv and the location of the maximum at about 3000 m (Fig. 9c3); (4) the weak and deep one, with the strength of about 10 Sv and the location of the maximum at about 3000 m (Fig. 9d3). Here the "strong (weak)" and "shallow (deep)" are defined in relative to the AMOC in the control run (Fig. 1c).

TABLE. 2. Parameter settings in different equilibrium experiments, in which the AMOC has different strength and structure

Experiments	AMOC	A_V (m^2 s^{-1})	A_H (m^2 s^{-1})	K_V (m^2 s^{-1})	K_H (m^2 s^{-1})
Ctrl	20 Sv, 1500 m	15	2.0×10^9	2.1×10^{-4}	3.0×10^3
Strong-Shallow	30 Sv, 1000 m	2	4.0×10^8	1.75×10^{-4}	7.0×10^3
Weak-Shallow	10 Sv, 1000 m	3	2.0×10^9	6.5×10^{-5}	3.0×10^3
Strong-Deep	30 Sv, 3000 m	600	3.0×10^8	6.65×10^{-4}	6.0×10^3
Weak-Deep	10 Sv, 3000 m	1000	2.0×10^9	1.43×10^{-4}	3.0×10^3

Corresponding to four different AMOC, the temperature and salinity have four different structures too (Figs. 9a1-d1, 9a2-d2). A stronger AMOC (Figs. 9a3, c3) is usually consistent with a more saline subpolar ocean (Figs. 9a2, c2). A deeper penetration of the downward branch of AMOC (Figs. 9c3, d3) is also consistent with a deeper downward mixing of subpolar surface water (Figs. 9c2, d2). The effect of temperature on the AMOC (Figs. 9a1-d1) always offsets that of salinity on the AMOC (Figs. 9a2-d2), which structure appears to be shaped as a result of the AMOC behavior.

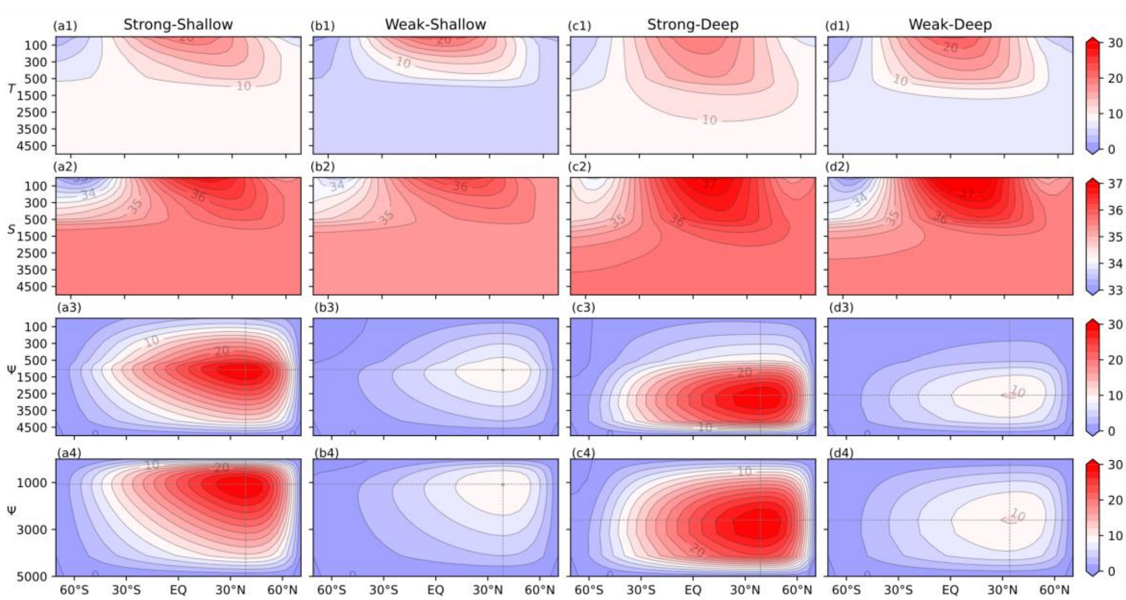

FIG. 9. Same as Fig. 1, but for four different equilibrium states of ocean buoyancy and the AMOC: (a) Strong-Shallow, (b) Weak-Shallow, (c) Strong-Deep, (d) Weak-Deep. Panels from upper to bottom show the equilibrium temperature, salinity, and AMOC, respectively.

Figure 10 illustrates the response of the AMOC to both white-noise and red-noise forcings in four different situations. Consistent with theoretical studies (Li and Yang 2022; Yang et al. 2024a), a stronger climatological AMOC leads to a shorter turnover time of ocean basin and thus a shorter MCO. Similarly, a shallower AMOC also leads to a shorter MCO due to a smaller upper ocean volume. Specifically, the principal oscillation period of AMOC in experiment Strong-Shallow is about 100 years (red curve, Figs. 10b, d), much shorter than the 300-year period in control run (black curve, Figs. 10b, d) and 400-year period in experiment Weak-Shallow (blue curve, Figs. 10b, d). Similarly, the principal period of AMOC in experiment Strong-Deep is about 400 years (green curve, Figs. 10b, d), much shorter than the 1000-year period in experiment Weak-Deep (orange curve, Figs. 10b, d). The ratios of period among them are approximately 120/450 for the shallow cases and 410/1120 for the deep cases, which roughly align with the ratios of climatological AMOC strength of 10.02/29.9 for shallow experiments and 10.12/29.7 for deep experiments. As far as the effect of AMOC structure is concerned, the principal oscillation period of AMOC in Strong-Shallow (red curve, Figs. 10b, d) is only one fourth of that in Strong-Deep (green curve, Figs. 10b, d), because of much smaller upper-ocean volume in the former than that in the latter. It is interesting to notice that the millennial oscillation appears in experiment Weak-Shallow, which is shown more clearly in experiments under red-noise forcing (orange curve, Fig. 10c).

Power spectra of the AMOC in red-noise experiments closely resemble those in white-noise experiments (Figs. 10b, d). However, in red-noise experiments, high-frequency variabilities of the AMOC are significantly reduced compared to those in white-noise experiments (Figs. 10a, b). This results in a clearer millennial oscillation in the former than in the latter.

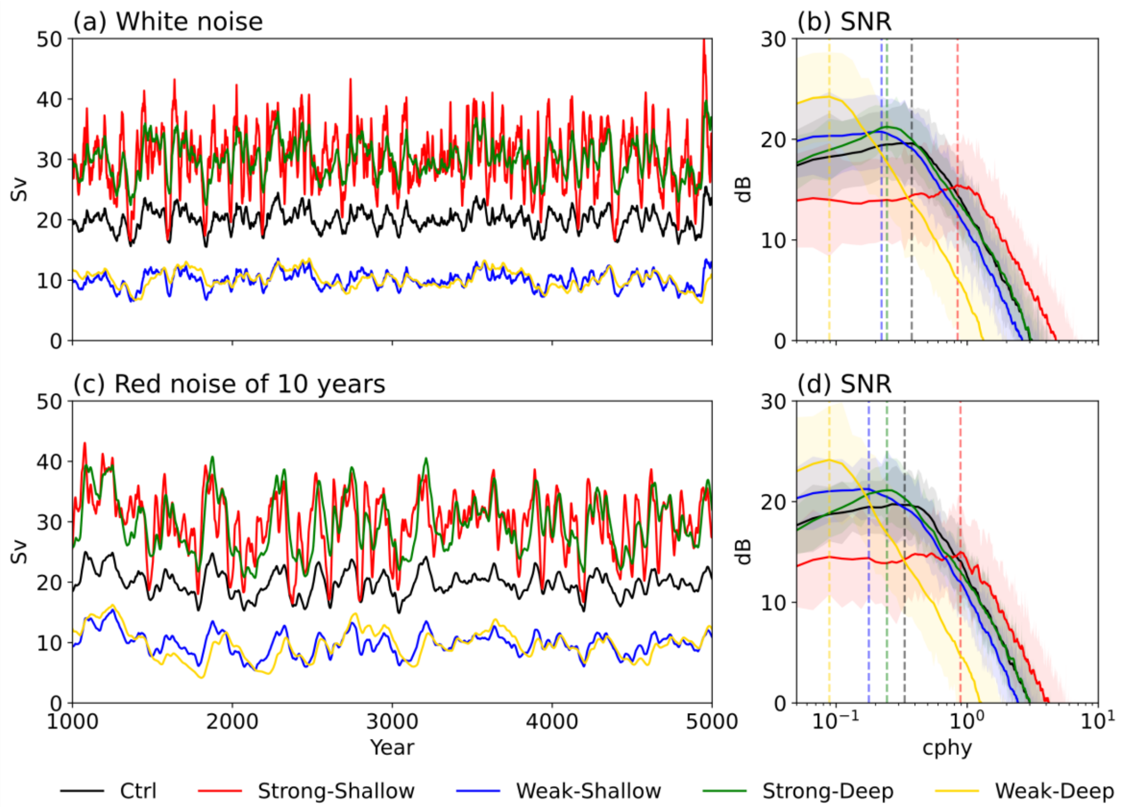

FIG. 10. (a) Time series of AMOC index (units: Sv) in control run (black) and four sensitivity experiments, forced by white-noise freshwater flux. No temporal filter is applied to the AMOC index. (b) Signal-to-noise power spectra (units: dB) of the AMOC. Thick curves represent the ensemble mean of 50 realizations that forced by white noise. Pale shadows demonstrate the spread of the 50 realizations. Red, blue, green and orange curves are for experiments Strong-Shallow, Weak-Shallow, Strong-Deep and Weak-Deep, respectively. Vertical dashed lines mark the location of peak frequency. (c)-(d) are same as (a)-(b), but for experiments forced by red-noise with an e-folding time of 10 years. The x-coordinate in (b)-(d) represents frequency with unit of cycles per hundred years (cphy).

5. Role of wind-driven circulation

In reality the AMOC consists of the buoyancy-driven thermohaline circulation and the wind-driven circulation in the tropical-extratropical ocean. Although the wind-driven component plays a minor role in the AMOC, its role in the internal low-frequency oscillation still needs to be evaluated. This can be easily done by using the simplified ocean model. Here we simply introduce Ekman velocity into the meridional velocity of Eqs. (2)-(3) to incorporate the effect of wind forcing:

$$v_1 = v_0 + v_e \tag{7}$$

where v_0 is the meridional velocity in Eqs. (2)-(3) that only include the thermohaline effect, v_e is Ekman velocity in Ekman layer. The meridional Ekman transport $V_E = -\frac{\tau_x}{\rho_0 f}$, where τ_x is zonal wind stress. τ_x can be parameterized by surface wind speed, which can be obtained from surface air temperature based on the thermal wind relation (Vallis 2017). Neglecting the minimal difference between surface air temperature and SST, we can finally have:

$$\tau_x = \rho_a C_D |u| u \approx \frac{gh\rho_a C_D |u|}{fT_0} \frac{\partial SST}{\partial y} \tag{8}$$

Therefore,

$$V_E = -\frac{\tau_x}{\rho_0 f} \approx -\frac{gh\rho_a C_D |u|}{f^2 \rho_0 T_0} \frac{\partial SST}{\partial y} \sim -\tau_0 \frac{\partial SST}{\partial y} \tag{9}$$

$$v_e \approx \frac{V_E}{D_e} \sim -\frac{\tau_0}{D_e} \frac{\partial SST}{\partial y} \tag{10}$$

where u is zonal wind speed, ρ_0 and ρ_a are reference density of ocean and atmosphere, respectively, h is the height of the atmospheric boundary layer, C_D is the drag coefficient, T_0 is reference SST. Thus, the relationship between Ekman transport and SST is established. Here, we define a “bulk” wind stress parameter $\tau_0 = \frac{gh\rho_a C_D |u|}{f^2 \rho_0 T_0}$, representing the resultant effect of the atmospheric boundary layer on the ocean surface, which can be tuned deliberately to obtain a reasonable (or control the strength of) wind-driven circulation. Notice that we assume a uniform v_e in the Ekman layer D_e in Eq. (10), neglecting the effect of Ekman spiral. In this work, D_e is given as a constant of 50 m.

Eqs. (8)-(10) suggest that a poleward SST gradient ($-\frac{\partial SST}{\partial y} > 0$) leads to an easterly wind ($\tau_x < 0$), and thus a northward Ekman transport ($V_E > 0$). Physically, we can simply understand this as follows: high (low) temperature in the tropics (extratropics) drives a normal clockwise Hadley Cell, and therefore generates easterlies in the tropics due to the Coriolis effect on the lower southward branch of the Hadley Cell, which in turn drives a northward Ekman flow. A stronger poleward SST gradient will result in a stronger northward Ekman transport, which, in turn, would reduce the poleward SST gradient. This is negative feedback between the SST gradient and the wind-driven circulation.

Using the climatological SST in the control run of Section 2 (Fig. 1a), the initial value of v_e can be obtain. With the time-forward integration of the model, v_e can affect T, S and thus ψ, and in turn, be renewed using calculated T at later time-step. This is actually an air-sea coupling process, providing with that the atmosphere responses to the ocean changes instantly. Similar to the procedures in experiments having only thermohaline circulation, a 5000-year control run with addition of wind-driven circulation is first performed, and then white-noise stochastic experiments are integrated for 5000 years. 50 ensemble experiments are conducted with 50 different white noises. The last 4500 years annual mean data are used for analyses.

Figure 11a illustrates the equilibrium AMOC after incorporating the wind-driven circulation. The wind-driven overturning circulation shown in Fig. 11b is obtained by subtracting the AMOC in Fig. 1c from Fig. 11a, which exhibits a symmetric structure to the equator. Under the bulk wind stress parameter τ_0 of around 5×10^3 m^3 °C^{-1} s^{-1}, the wind-driven overturning circulation has the maximum value of about 5 Sv, occupying the upper 1000 m ocean, consistent with the reality in the tropical Atlantic. The inclusion of wind-driven circulation does not lead to remarkable changes in both the strength and structure of the thermohaline component of AMOC, if the wind-driven circulation is managed well. However, a southward transport emerges in the upper ocean of Southern Hemisphere, forming a weak, reversed overturning circulation (Fig. 11a).

Inclusion of the wind-driven circulation does not affect the period and amplitude of the AMOC MCO either. Figure 11c shows that the power spectra curves of the AMOC with/without the wind-driven circulation are nearly identical. However, under closer inspection it appears that the oscillation amplitude of on multicentennial timescales (0.2–0.5 cphy) is weakened slightly, while oscillation amplitude on shorter timescales (>1.0 cphy) is enhanced slightly, when the wind-driven circulation is included. This occurs because there is a simple ocean-atmosphere coupling with the inclusion of the Ekman dynamics, which amounts to include an atmosphere process with a fast timescale, tending to promote high-frequency variabilities while suppress low-frequency variabilities.

In fact, there would be no MCO at all if there is only wind-driven overturning circulation in the ocean, confirmed by experiment with only wind-driven circulation considered (Fig. 12). In experiment of Fig. 12, we suppress the thermohaline circulation by simply configuring the parameters as A_V=10 m^2 s^{-1}, A_H=5×10^8 m^2 s^{-1}, K_V=1.0×10^{-5} m^2 s^{-1} and K_H=1.0×10^3 m^2 s^{-1}. The symmetric wind-driven overturning cell is obtained (Fig. 12a), which closely resembles the residual circulation shown in Fig. 11b. Just as expected, the power spectrum of the wind-driven cell shows no specific peak in centennial-millennial timescale (Fig. 12b).

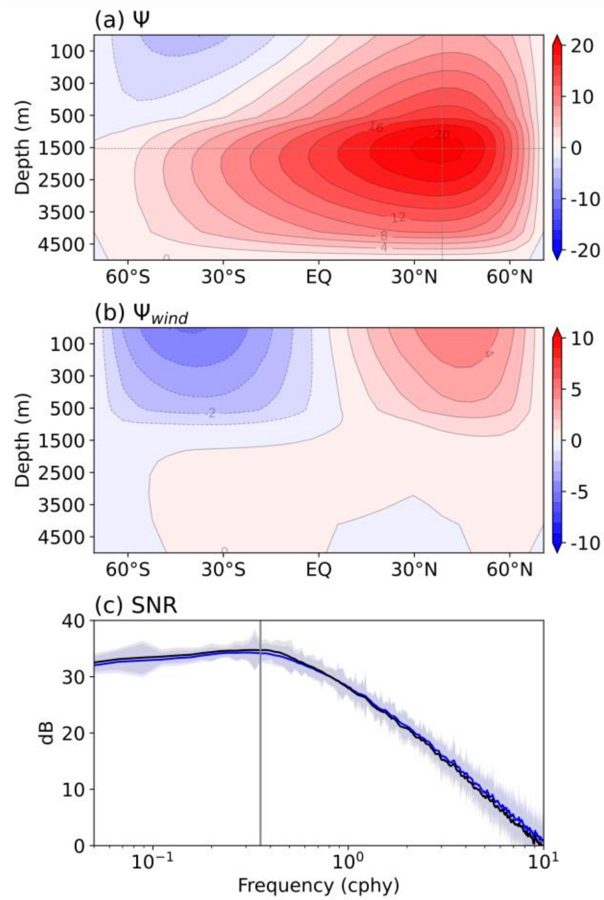

FIG. 11. (a) Equilibrium AMOC in the control run with the wind-driven circulation included (units: Sv), (b) difference between (a) and the AMOC in Fig. 1c, i.e., the wind-driven overturning circulation (units: Sv), and (c) power spectra of the AMOC forced by white noise freshwater flux (units: dB). Blue (black) curves represent the AMOC with (without) the wind-driven component. The pale shading represents the spread of 50 ensemble experiments. Vertical dashed lines mark the location of peak frequency.

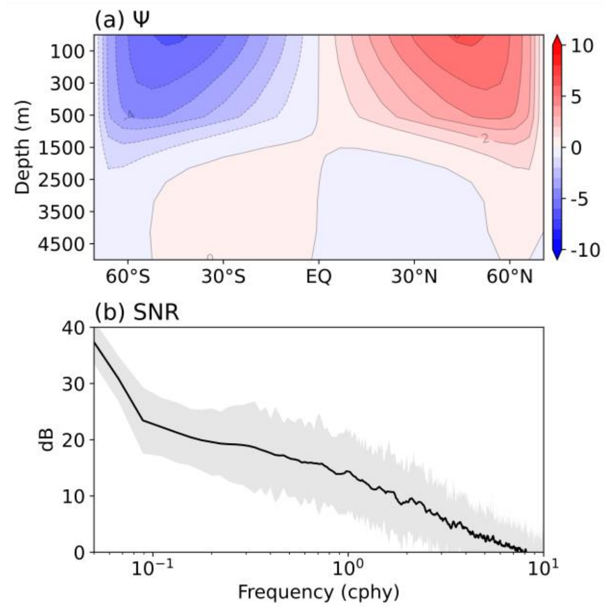

FIG. 12. (a) Equilibrium wind-driven overturning circulation in experiment without thermohaline circulation (units: Sv), and (b) power spectrum of the wind-driven overturning circulation forced by white noise freshwater flux (units: dB). Black curve represents the ensemble mean of 50 realizations and the pale shading represents the spread of 50 ensemble experiments.

6. Summary and discussion

In this study, we investigate the AMOC MCO using a simplified two-dimensional ocean model. Our goal is to bridge the gap between theoretical models and complex coupled climate models by providing clearer physical insights and allowing for more extensive sensitivity experiments. The model successfully simulates sustained AMOC MCO under stochastic freshwater forcing. The oscillation is primarily driven by the tropical-subpolar advection feedback. The results suggest that AMOC MCO is an intrinsic feature of the Atlantic Ocean. Sensitivity experiments indicate that the period of the AMOC MCO is primarily controlled by the strength and structure of the climatological AMOC. Specifically, a stronger AMOC leads to a shorter oscillation period, consistent with a faster turnover time of the ocean. A deeper AMOC maximum results in a longer oscillation period due to the larger effective ocean volume involved in the overturning circulation. Under sufficiently weak AMOC conditions, the oscillation timescale can extend to millennial scales.

The AMOC MCO is sustained through a combination of positive and negative feedbacks. Perturbation advection of mean salinity plays a positive feedback role in the subpolar deep-water formation region, which enhances AMOC anomalies and sustains the oscillation. Mean advection of salinity anomaly plays a negative feedback role, gradually damping AMOC anomalies and driving phase transitions. Temperature anomalies tend to counteract the salinity-driven density anomalies, reinforcing the dominance of salinity in AMOC variability.

Including a wind-driven overturning circulation has little effect on the AMOC MCO period but slightly modifies its amplitude. Specifically, it tends to suppress low-frequency variability while enhancing high-frequency variability, consistent with the introduction of an atmospheric process with a faster timescale. Our results also reaffirm that North Atlantic-originated processes dominate the AMOC MCO (Yang et al. 2024b). While Arctic Ocean-originated freshwater transport and sea-ice-related processes influence the salinity budget, their effects largely compensate for each other, reducing their net impact on AMOC variability. This challenges previous studies that emphasize the Arctic's control over AMOC MCO (Jiang et al. 2021; Meccia et al. 2022; Mehling et al. 2022).

Our study employs a zonal-mean two-dimensional ocean model, which removes wave dynamics and filters out high-frequency internal variability associated with eddy and gyre dynamics. This design ensures that low-frequency variability, such as the AMOC MCO, emerges more clearly, making it easier to identify the underlying mechanisms. While this simplification is useful for isolating key processes, it also implies that certain dynamical interactions, such as eddy-driven salinity transport, are not explicitly resolved. Future studies using three-dimensional models may help assess the role of these missing dynamics.

Our results demonstrate that model parameters strongly influence the AMOC MCO period and amplitude. The critical parameters include eddy viscosity and diffusivity coefficients, which regulate the strength and structure of the AMOC, and thus the properties of MCO (Mysak et al. 1993; Schmidt and Mysak 1996). Surface boundary conditions, such like use of fixed or interactive surface freshwater flux, can also alter the feedback mechanisms sustaining AMOC variability. While our sensitivity experiments provide useful constraints, further work is needed to explore how different parameterizations affect AMOC MCO in fully coupled models.

Our analysis reveals that the positive and negative phases of the AMOC MCO are not symmetric. This asymmetry likely arises because the MCO is stochastically excited. Additionally, nonlinearities in the response of the oceanic circulation to salinity and temperature anomalies may contribute to asymmetry. Future work could investigate whether this asymmetry persists in fully coupled models and whether it has implications for predictability.

Our findings align with recent theoretical studies that emphasize the positive salinity advection feedback as a key driver of AMOC MCO (Li and Yang 2022; Yang et al. 2024a). They also suggest that Atlantic-only models, despite their simplifications, may capture the most essential processes governing low-frequency AMOC variability (Yang et al. 2024b). Compared to box models, the two-dimensional simple model can reveal more detailed features, while compared to coupled models, it significantly reduces computational costs. However, due to the challenges in simulating the deep-water formation process in the Southern Ocean within a simple model, the equilibrium state and its relevance to three-dimensional or coupled models require further exploration. Current efforts with a three-dimensional planetary geostrophic ocean model are on the way, aiming to investigate the AMOC MCO in an extended version of the "simple model", thereby offering a deeper understanding of the coupled model simulations and theoretical research of AMOC MCO.

Acknowledgements

This research is jointly supported by the NSF of China (Nos. 42230403, 42288101 and 41725021) and by the foundation at the Shanghai Frontiers Science Centre of Atmosphere-Ocean Interaction of Fudan University.

Data Availability Statement

All data used in this study are available upon request.

Conflict of interest

The authors have no relevant financial or non-financial interests to disclose.

REFERENCES

Askjær, T. G., and Coauthors, 2022: Multi-centennial Holocene climate variability in proxy records and transient model simulations. *Quat. Sci. Rev.*, **296,** 107801, https://doi.org/10.1016/j.quascirev.2022.107801.

Binford, M. W., A. L. Kolata, M. Brenner, J. W. Janusek, M. T. Seddon, M. Abbott, and J. H. Curtis, 1997: Climate Variation and the Rise and Fall of an Andean Civilization. *Quat. Res.*, **47,** 235-248, https://doi.org/10.1006/qres.1997.1882.

Cao, N., Q. Zhang, K. E. Power, F. Schenk, K. Wyser, and H. Yang, 2023: The role of internal feedbacks in sustaining multi-centennial variability of the Atlantic Meridional Overturning Circulation revealed by EC-Earth3-LR simulations. *Earth Planet. Sci. Lett.*, **621,** 118372, https://doi.org/10.1016/j.epsl.2023.118372.

Chabaud, L., M. F. Sánchez Goñi, S. Desprat, and L. Rossignol, 2014: Land–sea climatic variability in the eastern North Atlantic subtropical region over the last 14,200 years: atmospheric and oceanic processes at different timescales. *Holocene*, **24,** 787-797, https://doi.org/10.1177/0959683614530439.

Chapman, M. R., and N. J. Shackleton, 2000: Evidence of 550-year and 1000-year cyclicities in North Atlantic circulation patterns during the Holocene. *Holocene*, **10,** 287-291, https://doi.org/10.1191/095968300671253196.

Collins, M., and B. Sinha, 2003: Predictability of decadal variations in the thermohaline circulation and climate. *Geophys. Res. Lett.*, **30,** 1306, https://doi.org/10.1029/2002GL016504.

Delworth, T. L., and F. Zeng, 2012: Multicentennial variability of the Atlantic meridional overturning circulation and its climatic influence in a 4000 year simulation of the GFDL CM2. 1 climate model. *Geophys. Res. Lett.*, **39,** L13702, https://doi.org/10.1029/2012GL052107.

Hirschi, J. J.-M., and Coauthors, 2020: The Atlantic Meridional Overturning Circulation in High-Resolution Models. *J. Geophys. Res. Oceans*, **125,** e2019JC015522, https://doi.org/10.1029/2019JC015522.

Hodell, D. A., J. H. Curtis, and M. Brenner, 1995: Possible role of climate in the collapse of Classic Maya civilization. *Nature*, **375,** 391-394, https://doi.org/10.1038/375391a0.

Jiang, W., G. Gastineau, and F. Codron, 2021: Multicentennial Variability Driven by Salinity Exchanges Between the Atlantic and the Arctic Ocean in a Coupled Climate Model. *J. Adv. Model. Earth Syst.*, **13,** e2020MS002366, https://doi.org/10.1029/2020MS002366.

Kissel, C., A. Van Toer, C. Laj, E. Cortijo, and E. Michel, 2013: Variations in the strength of the North

Atlantic bottom water during Holocene. *Earth Planet. Sci. Lett.*, **369,** 248-259, https://doi.org/10.1016/j.epsl.2013.03.042.

Li, Y., and H. Yang, 2022: A Theory for Self-Sustained Multicentennial Oscillation of the Atlantic Meridional Overturning Circulation. *J. Climate*, **35,** 5883-5896, https://doi.org/10.1175/jcli-d-21-0685.1.

Marotzke, J., P. Welander, and J. Willebrand, 1988: Instability and multiple steady states in a meridional-plane model of the thermohaline circulation. *Tellus*, **40,** 162-172, https://doi.org/10.3402/tellusa.v40i2.11790.

McDermott, F., D. P. Mattey, and C. Hawkesworth, 2001: Centennial-scale Holocene climate variability revealed by a high-resolution speleothem δ18O record from SW Ireland. *Science*, **294,** 1328-1331, https://doi.org/10.1126/science.1063678.

Meccia, V. L., R. Fuentes-Franco, P. Davini, K. Bellomo, F. Fabiano, S. Yang, and J. von Hardenberg, 2022: Internal multi-centennial variability of the Atlantic Meridional Overturning Circulation simulated by EC-Earth3. *Climate Dyn.*, **60,** 1-18, https://doi.org/10.1007/s00382-022-06534-4.

Mehling, O., K. Bellomo, M. Angeloni, C. Pasquero, and J. Von Hardenberg, 2022: High-latitude precipitation as a driver of multicentennial variability of the AMOC in a climate model of intermediate complexity. *Climate Dyn.*, **61,** 1519-1534, https://doi.org/10.1007/s00382-022-06640-3.

Mikolajewicz, U., and E. Maier-Reimer, 1990: Internal secular variability in an ocean general circulation model. *Climate Dyn.*, **4,** 145-156, https://doi.org/10.1007/BF00209518.

Moffa-Sánchez, P., and Coauthors, 2019: Variability in the Northern North Atlantic and Arctic Oceans Across the Last Two Millennia: A Review. *Paleoceanogr. Paleoclimatol.*, **34,** 1399-1436, https://doi.org/10.1029/2018PA003508.

Msadek, R., and C. Frankignoul, 2009: Atlantic multidecadal oceanic variability and its influence on the atmosphere in a climate model. *Climate Dyn.*, **33,** 45-62, https://doi.org/10.1007/s00382-008-0452-0.

Mysak, L. A., T. F. Stocker, and F. Huang, 1993: Century-scale variability in a randomly forced, two-dimensional thermohaline ocean circulation model. *Climate Dyn.*, **8,** 103-116, https://doi.org/10.1007/BF00208091.

Newby, P. E., B. N. Shuman, J. P. Donnelly, K. B. Karnauskas, and J. Marsicek, 2014: Centennial-to-millennial hydrologic trends and variability along the North Atlantic Coast, USA, during the Holocene. *Geophys. Res. Lett.*, **41,** 4300-4307, https://doi.org/10.1002/2014GL060183.

Oppo, D. W., J. F. McManus, and J. L. Cullen, 2003: Deepwater variability in the Holocene epoch. *Nature*, **422,** 277, https://doi.org/10.1038/422277b.

Park, W., and M. Latif, 2008: Multidecadal and multicentennial variability of the meridional overturning circulation. *Geophys. Res. Lett.*, **35,** L22703, https://doi.org/10.1029/2008GL035779.

Proctor, C., A. Baker, and W. Barnes, 2002: A three thousand year record of North Atlantic climate. *Climate Dyn.*, **19,** 449-454, https://doi.org/10.1007/s00382-002-0236-x.

Rahmstorf, S., 2002: Ocean circulation and climate during the past 120,000 years. *Nature*, **419,** 207-214, https://doi.org/10.1038/nature01090.

——, 2006: Thermohaline ocean circulation. *Encyclopedia of quaternary sciences*, S. A. Elias, Ed., Elsevier, 739-750.

Roebber, P. J., 1995: Climate variability in a low-order coupled atmosphere-ocean model. *Tellus*, **47,** 473-494, https://doi.org/10.1034/j.1600-0870.1995.t01-3-00006.x.

Schmidt, G. A., and L. A. Mysak, 1996: The stability of a zonally averaged thermohaline circulation model. *Tellus A*, **48,** 158-178, https://doi.org/10.1034/j.1600-0870.1996.00009.x.

Srokosz, M., and Coauthors, 2012: Past, present, and future changes in the Atlantic meridional overturning circulation. *Bull. Amer. Meteor. Soc.*, **93,** 1663-1676, https://doi.org/10.1175/BAMS-D-11-00151.1.

Stocker, T. F., and L. A. Mysak, 1992: Climatic fluctuations on the century time scale: A review of high-resolution proxy data and possible mechanisms. *Climate Change*, **20,** 227-250, https://doi.org/10.1007/BF00139840.

Stocker, T. F., L. A. Mysak, and D. G. Wright, 1992: A zonally averaged, coupled ocean-atmosphere model for paleoclimate studies. *J. Climate*, **5,** 773-797, https://doi.org/10.1175/1520-0442(1992)005<0773:AZACOA>2.0.CO;2.

Stommel, H., 1961: Thermohaline convection with two stable regimes of flow. *Tellus*, **13,** 224-230, https://doi.org/10.1111/j.2153-3490.1961.tb00079.x.

Thornalley, D. J., and Coauthors, 2013: Long-term variations in Iceland–Scotland overflow strength during the Holocene. *Climate Past*, **9,** 2073-2084, https://doi.org/10.5194/cp-9-2073-2013.

Vallis, G. K., 2017: *Atmospheric and Oceanic Fluid Dynamics.* Cambridge University Press, 946 pp.

Walland, D., S. Power, and A. Hirst, 2000: Decadal climate variability simulated in a coupled general circulation model. *Climate Dyn.*, **16,** 201-211, https://doi.org/10.1007/s003820050013.

Welander, P., 1982: A simple heat-salt oscillator. *Dyn. Atmos. Oceans*, **6,** 233-242, https://doi.org/10.1016/0377-0265(82)90030-6.

Yang, J., and J. D. Neelin, 1993: Sea-ice interaction with the thermohaline circulation. *Geophys. Res. Lett.*, **20,** 217-220, https://doi.org/10.1029/92GL02920.

Yang, K., H. Yang, and Y. Li, 2024a: A Theory for Self-Sustained Multicentennial Oscillation of the Atlantic Meridional Overturning Circulation. Part II: Role of Temperature. *J. Climate*, **37,** 913-926, https://doi.org/10.1175/JCLI-D-22-0755.1.

Yang, K., H. Yang, Y. Li, and Q. Zhang, 2024b: North Atlantic Ocean-Originated Multicentennial Oscillation of the AMOC: A Coupled Model Study. *J. Climate*, **37,** 2789-2801, https://doi.org/10.1175/JCLI-D-23-0422.1.